Deposited via The University of Sheffield.

White Rose Research Online URL for this paper:
https://eprints.whiterose.ac.uk/id/eprint/239211/

Version: Accepted Version

Article:

Qi, M.-Y., Tan, C.-L., Tang, Z.-R. et al. (2026) Efficient methanol upcycling to ethylene glycol and glycolaldehyde via divergent C−C coupling synthesis. Nature Communications. ISSN: 2041-1723

https://doi.org/10.1038/s41467-026-69656-x

Efficient methanol upcycling toward divergent C–C coupling synthesis by radical homo-coupling and addition-elimination pathway

Ming-Yu Qi,[1,2] Chang-Long Tan,[2] Zi-Rong Tang,*[,1,3] Marco Conte,[4] Yugang Sun,*[,5] and Yi-Jun Xu*[,2,3]

[1] School of Materials and Energy, University of Electronic Science and Technology of China, Chengdu 611731, P. R. China
[2] Institute of Fundamental and Frontier Sciences, University of Electronic Science and Technology of China, Chengdu 611731, P. R. China
[3] College of Chemistry, State Key Laboratory of Photocatalysis on Energy and Environment, Fuzhou University, Fuzhou 350116, P. R. China
[4] School of Mathematical and Physical Sciences, University of Sheffield, Sheffield, S3 7HF, UK
[5] Department of Chemistry, Temple University, 1901 North 13th Street, Philadelphia, Pennsylvania 19122, USA
* To whom correspondence should be addressed.
E-mail: zrtang@uestc.edu.cn; ygsun@temple.edu; yjxu@uestc.edu.cn

Abstract

Direct photocatalytic conversion of methanol into high-value multi-carbon chemicals through precisely controlled C–C coupling represents an extremely appealing but challenging goal. Herein, we demonstrate the efficient photoredox-driven dehydrocoupling of methanol into divergent synthesis of ethylene glycol (EG) and glycolaldehyde (GLD) concomitantly with H_2 production by structural regulation of atomically dispersed Ni species. We showcase distinctly different reaction pathway for divergent C–C coupling of methanol over two types of atomically dispersed Ni cocatalyst-decorated CdS quantum dots, namely those with single Ni atoms (Ni_1-CdS/SiO_2) and Ni clusters (Ni_n-CdS/SiO_2). The Ni_1-CdS/SiO_2 catalyst generates EG with a selectivity of 90% by a radical homo-coupling pathway, whereas the Ni_n-CdS/SiO_2 catalyst achieves a high selectivity of 96% towards GLD by a radical addition-elimination pathway with an impressive apparent quantum yield of 17.2%. This work not only offers a fascinating nonpetroleum route for the divergent C–C coupling synthesis of EG and GLD but also underscores the broad vista of modulating non-selective radicals toward selective transformation of methanol into multi-carbon products.

Introduction

Methanol, which can be sourced from diverse carbon resources, including CO_2, natural/shale gas, coal and biomass, functions as a vastly abundant one-carbon (C_1) building block in today's chemical industry[1-6]. Catalytic methanol transformation involves the activation/conversion of methanol into many types of value-added chemicals, in which the construction of C–C bond represents the most fascinating yet challenging reaction[1]. Presently, methanol conversions associated with C–C bond formation are mainly confined to dehydrative oligomerizations, such as industrial methanol-to-gasoline (MTG) and methanol-to-olefin (MTO) processes, which suffer from restricted selectivity towards target products[7-9]. Against the backdrop of escalating interest in the methanol economy, it is of urgency and great significance to develop novel and alternative routes for the transformation of

44 methanol via controllable C–C coupling with high reaction efficiency and selectivity.

45   In principle, the transformation of methanol inevitably involves the activation of either its α-C–H or
46 C–O/O–H bond[1,4]. Of note, the preferential activation of C–O/O–H bond in methanol usually brings
47 along value-reduced oxidation products, especially formaldehyde (HCHO) and even CO_2[10-12]. To access
48 two-carbon (C_2) products via C–C coupling, the selective activation of targeted α-C–H bond in
49 methanol is crucial but challenging[13-16]. Recent years have witnessed the application of metal sulfide
50 semiconductors as photocatalysts to selectively activate the inert α-C–H bond in methanol with the
51 O–H bond intact, thus affording high-reactive hydroxymethyl (•CH_2OH) radicals for the synthesis of
52 ethylene glycol (EG)[1,17-22]. Nevertheless, these previous catalytic systems not only encounter the trade-
53 off between activity and selectivity, but also fail to produce other value-added C_2 products because of
54 the pervasive difficulty in steering non-selective •CH_2OH radicals toward controllable C–C coupling
55 pathway for divergent synthesis of C_2 feedstocks. In particular, glycolaldehyde (GLD), a highly attractive
56 C_2 chemical with versatile applications[23-26], has usually been synthesized with low activity and
57 selectivity. These unsolved problems stem from the failure to efficiently manipulate the •CH_2OH
58 radical conversion pathway after the preferential activation and cleavage of α-C–H bond in methanol is
59 achieved. In such a scenario, upon overcoming α-C–H bond-breaking event, the precise regulation of
60 activity/selectivity by preferably steering non-selective •CH_2OH radical conversion route presents a
61 brand-new challenge in advancing methanol chemistry and holds great academic significance.

62   Herein, we report the unique ensemble of atomically dispersed Ni-decorated CdS quantum dots
63 (QDs) supported on spherical SiO_2 (Ni-CdS/SiO_2) for the tunable, high-performance photochemical C–C
64 coupling of methanol into EG and GLD integrated with concomitant H_2 production at ambient
65 conditions. The present CdS QDs can selectively activate the unreactive α-C–H bond in methanol with
66 the O–H group intact, thus affording sufficient high-reactive •CH_2OH radicals. Loading CdS QDs onto
67 the SiO_2 support not only regulates the dielectric environment of CdS QDs via the near-field scattering
68 promoted optical absorption model for enhanced light-capturing property[15,27,28], but also improves
69 their antiphotocorrosion ability and recyclability. Two types of atomically dispersed Ni species, single
70 Ni atoms for Ni_1-CdS/SiO_2 and Ni clusters for Ni_n-CdS/SiO_2, act as active sites to govern •CH_2OH radicals
71 conversion pathway for precisely tailoring the C–C coupling synthesis between EG and GLD formation
72 reaction, along with significantly enhanced activity. As an outcome, EG is generated with 90%
73 selectivity over the Ni_1-CdS/SiO_2 catalyst, and a high selectivity of 96% towards GLD is obtained over
74 the Ni_n-CdS/SiO_2 catalyst. Mechanistic insights by joint theoretical and experimental studies unveil that
75 the divergent synthesis of EG and GLD over Ni-CdS/SiO_2 originates from the single Ni atoms-assisted
76 homo-coupling of •CH_2OH radicals and Ni clusters-catalyzed radical addition-elimination mechanism,
77 respectively.

78

79 **Results**

80 **Preparation and characterization of Ni-CdS/SiO_2 with atomically dispersed Ni species**

81   The schematic diagram of the fabrication of atomically dispersed Ni-decorated CdS QDs supported
82 on spherical SiO_2 (Ni-CdS/SiO_2) is depicted in **Fig. 1a**. Initially, CdS QDs were prepared by a one-pot
83 synthesis using 3-mercaptopropionic acid (MPA) as capping molecule (**Supplementary Table 1**), and
84 then loaded onto the SiO_2 support (CdS/SiO_2) through an electrostatic self-assembly strategy.
85 Transmission electron microscopy (TEM) images afford the detailed insights into the microscopic
86 structures and morphologies of CdS/SiO_2 composite. In contrast to the smooth surface of SiO_2 sphere
87 (**Supplementary Fig. 1a** and **b**), the uniform distribution of CdS QDs can be distinctly identified on the

surface of SiO_2 sphere within the CdS/SiO_2 composite (**Fig. 1b**). Subsequently, photodeposition of Ni species onto CdS/SiO_2 was performed using $NiCl_2 \cdot 6H_2O$ as the precursor under 0.5 h of xenon-lamp irradiation. The CdS/SiO_2 composite contains abundant dangling –COOH groups originating from MPA, which serve to adsorb and anchor Ni^{2+} cations (**Supplementary Fig. 2**)[28,29]. The $Ni-CdS/SiO_2$ composites with different Ni loading contents were obtained by regulating the amount of Ni precursor (**Supplementary Table 2**, the two representative samples of $Ni_{0.1}-CdS/SiO_2$ and $Ni_{1.0}-CdS/SiO_2$ with the lowest and highest Ni loading amounts are denoted as Ni_1-CdS/SiO_2 and Ni_n-CdS/SiO_2, respectively). High-resolution TEM (HR-TEM, **Supplementary Fig. 1c** and **d**) analysis exhibits the ordered lattice fringe with a d-spacing of 0.335 nm, ascribed to the (111) crystal plane of cubic CdS[28]. No formation of Ni-derived nanoparticles is observed in high-resolution TEM images of both the Ni_1-CdS/SiO_2 and Ni_n-CdS/SiO_2, certifying that the Ni species in these two catalysts are both atomically dispersed on CdS/SiO_2. As illustrated in **Supplementary Fig. 1e**, elemental mapping results further validate the even dispersion of Cd, S and Ni elements throughout the SiO_2 support. From aberration-corrected high-angle annular dark-field scanning TEM (**Supplementary Fig. 3**), high-density bright dots assigned to the overlapped image contrast of Cd atom and Ni atom are observed in Ni_n-CdS/SiO_2, confirming the formation of Ni clusters.

To gain the local coordination structure of Ni species, X-ray absorption spectroscopy (XAS) measurements were performed. **Fig. 1c** shows the Ni K-edge X-ray absorption near-edge structure (XANES) spectra of Ni_1-CdS/SiO_2 and Ni_n-CdS/SiO_2 in reference to Ni foil and NiO. The threshold energy of Ni_1-CdS/SiO_2 falls between Ni foil and NiO, suggesting an electron-deficient state of $Ni^{\delta+}$ ($0 < \delta < 2$)[30,31], and that of Ni_n-CdS/SiO_2 is close to standard NiO, manifesting that the electronic state of Ni species in Ni_n-CdS/SiO_2 is approximate to +2[29,32], consistent with the X-ray photoelectron spectroscopy (XPS) results (**Supplementary Fig. 4** and **5**). As sketched in **Fig. 1d**, the extended X-ray absorption fine structure (EXAFS) spectrum of Ni_1-CdS/SiO_2 only features a prominent peak at 1.38 Å from Ni–O coordination, suggesting the formation of isolated Ni atom in Ni_1-CdS/SiO_2[28,33]. For Ni_n-CdS/SiO_2, an additional peak at about 2.69 Å from Ni–Ni coordination emerges, corroborating the formation of Ni clusters[29]. The trend can also be clearly resolved from the wavelet transform on Ni K-edge EXAFS oscillations (**Fig. 1e**,**f** and **Supplementary Fig. 6**). From the fitting structural parameters (**Fig. 1g**,**h**, **Supplementary Fig. 7** and **Supplementary Table 3**), the Ni-O coordination number in Ni_1-CdS/SiO_2 is evaluated to be 2.6 ± 0.2, indicating the Ni single atoms with a $Ni-O_3$ moiety. In addition, the Ni-O and Ni–Ni coordination numbers of Ni clusters in Ni_n-CdS/SiO_2 are calculated to be 6.4 ± 0.2 and 3.5 ± 0.3, respectively. The above results elucidate that these two catalysts exhibit distinct difference in electronic structure as well as in coordination environment. With the further aid of density functional theory (DFT) optimization calculations, the most stable structures of Ni_1-CdS/SiO_2 and Ni_n-CdS/SiO_2 are sketched in **Supplementary Fig. 8**.

Selective dehydrocoupling of methanol to produce EG or GLD

Subsequently, we evaluated the application of $Ni-CdS/SiO_2$ for dehydrocoupling of methanol to EG or GLD integrated with H_2 evolution, in one tunable photoredox catalytic system (**Fig. 2a**). As displayed in **Fig. 2b** and **c**, the blank CdS QDs exhibit low EG and H_2 production rates, reaching only 1.9 and 2.8 mmol g_{Ni-CdS}^{-1} h^{-1}, respectively. Compared to bare CdS QDs, CdS/SiO_2 presents much higher EG formation rate of 4.1 mmol g_{Ni-CdS}^{-1} h^{-1}; meanwhile, the production rate of H_2 improves from 2.8 to 6.4 mmol g_{Ni-CdS}^{-1} h^{-1}, which is attributed to the distinctly enhanced optical absorption correlated to the scattering resonances of the SiO_2 supports (**Supplementary Fig. 9**)[15,28]. Upon decorating with Ni, the Ni_1-CdS/SiO_2 exhibits significantly enhanced EG formation rate (16.8 mmol g_{Ni-CdS}^{-1} h^{-1}) by 3.1 times as

132 compared to CdS/SiO$_2$, along with a high EG selectivity of 90% (**Supplementary Fig. 10-14**). Remarkably,
133 as the Ni loading increases, the selective product in the dehydrocoupling of methanol transitions from
134 EG to GLD (**Supplementary Fig. 10-14**). Consequently, over Ni$_n$-CdS/SiO$_2$, a GLD evolution rate of 24.1
135 mmol g$_{Ni-CdS}^{-1}$ h^{-1} is achieved with an excellent selectivity of 96% (**Fig. 2b**). In addition, the production
136 of H$_2$ increases along with Ni loading amount, and the ratios of electrons (consumed for the reduction
137 product H$_2$) to holes (consumed for the oxidation products EG/GLD/HCHO) over different catalysts are
138 calculated to be approximately 1:1 (**Supplementary Table 4**), indicating a stoichiometric
139 dehydrocoupling reaction. It is noteworthy that HCHO (a major by-product of methanol oxidation)
140 consistently maintains an exceedingly low evolution rate (< 1.2 mmol g$_{Ni-CdS}^{-1}$ h^{-1}) in the current
141 catalysis system. In addition, the optimized apparent quantum yields (AQYs) of 12.3% for EG and 17.2%
142 for GLD are attained over Ni$_1$-CdS/SiO$_2$ and Ni$_n$-CdS/SiO$_2$ respectively, at λ = 370 nm (**Fig. 2d**). Compared
143 with previously reported catalytic systems (**Supplementary Table 5**)[1,17-22], this work represents the first
144 report on photocatalytic methanol coupling for the divergent synthesis of EG and GLD concomitantly
145 with H$_2$ production.

146   The stability of Ni-CdS/SiO$_2$ was then investigated by cycle experiments, as shown in **Fig. 2e** and **f**.
147 After five repeated tests of totaling 50 h, the catalytic performance for EG (or GLD) and H$_2$
148 coproduction over Ni$_1$-CdS/SiO$_2$ (or Ni$_n$-CdS/SiO$_2$) remains relatively stable; nevertheless, that of
149 unsupported CdS QDs decreases by 42.8% for EG and 43.6% for H$_2$ (**Supplementary Fig. 15**). The high-
150 resolution XPS analysis in **Supplementary Fig. 16** illustrates the good maintenance of element
151 composition in used Ni$_1$-CdS/SiO$_2$ compared with fresh Ni$_1$-CdS/SiO$_2$. In addition, element leakage after
152 10 h of continuous light irradiation was evaluated. As shown in **Supplementary Table 6**, only slight Cd^{2+}
153 leakages of 1.34 µg and 1.12 µg are observed in Ni$_1$-CdS/SiO$_2$ and Ni$_n$-CdS/SiO$_2$ respectively, which are
154 much lower than those of bare CdS QDs (7.35 µg for Cd^{2+}). These results collectively illustrate that this
155 self-assembly strategy suppresses the photocorrosion of CdS QDs and facilitates the recovery of CdS
156 QDs from the reaction solvent. Furthermore, taking into account that single atoms may aggregate
157 under light irradiation[34,35], we performed additional XAS characterizations on Ni$_1$-CdS/SiO$_2$ after five
158 consecutive reaction cycles. Notably, in the EXAFS spectrum of the used Ni$_1$-CdS/SiO$_2$ after 50 h of light
159 exposure, an additional weak peak emerges at approximately 2.64 Å from Ni–Ni coordination
160 (**Supplementary Fig. 17**), indicating the partial agglomeration of single Ni atoms during the prolonged
161 light irradiation (**Supplementary Table 7**), which accounts for the slight decrease in EG selectivity (**Fig.
162 2e**).

Mechanism insight for dehydrocoupling of methanol

164 Given that the charge separation dynamics usually restricts the catalytic performance, photo-
165 electrochemical characterizations were first carried out. As depicted in **Supplementary Fig. 18a**, the
166 transient photocurrent densities of these samples increase in the following sequence: CdS/SiO$_2$ < Ni$_1$-
167 CdS/SiO$_2$ < Ni$_n$-CdS/SiO$_2$, implying that decorating CdS/SiO$_2$ with Ni species remarkably enhances the
168 charge separation efficiency, which was further verified by the electrochemical impedance
169 spectroscopy (EIS) analysis (**Supplementary Fig. 18b**). These results distinctly indicate that the
170 incorporation of atomically dispersed Ni species into CdS/SiO$_2$ facilitates the conversion of methanol to
171 EG or GLD for a significantly boosted activity by expediting the separation and transfer of
172 photogenerated electrons and holes.

173   To probe the reaction mechanism of methanol coupling to EG/GLD integrated with H$_2$ evolution in
174 the present catalytic system, the band structure of CdS QDs was measured. As displayed in **Fig. 3a**,
175 Tauc plot indicates the bandgap energy (E$_g$) of CdS QDs to be around 2.48 eV. The conduction-band (CB)

176 edge of CdS QDs is measured with the value of −0.72 V vs NHE based on the Mott–Schottky curve, and
177 the valence-band (VB) edge of CdS QDs is thus calculated to be 1.76 V vs NHE. Taking into account
178 both the limited interfacial contact between Ni species and CdS QDs enabled by the capping molecule
179 of MPA and the low Ni loading amount (0.1 to 1%)[36-38], anchoring Ni species is insufficient to induce
180 significant alterations to the band structure of CdS QDs. In addition, the redox potential of methanol is
181 evaluated at about 0.61 V vs NHE by virtue of the cyclic voltammograms (**Supplementary Fig. 19**)[39-41].
182 Obviously, the CB edge of CdS QDs is higher than $E(H^+/H_2)$ (−0.41 V vs. NHE), and the VB edge is lower
183 than $E(\text{methanol/methanol}^{\bullet+})$, which fulfills the thermodynamic constraints for the synchronous
184 occurrence of these two half-reactions (**Fig. 3b**)[11].

185 To further decipher the function-oriented effects of Ni decoration with regard to the selectivity
186 regulation in methanol coupling to EG and GLD, we performed a set of control experiments. As shown
187 in **Supplementary Fig. 20**, the catalytic performance (including EG, GLD and H_2 production rates as well
188 as EG/GLD selectivity) of both Ni_{1-IM}-CdS/SiO$_2$ and Ni_{n-IM}-CdS/SiO$_2$ synthesized through impregnation
189 method is significantly lower than that of the corresponding Ni_1-CdS/SiO$_2$ and Ni_n-CdS/SiO$_2$, suggesting
190 the unique structural advantages of atomically dispersed Ni species afforded by the photodeposition
191 strategy. In the absence of catalyst or light, the photocatalytic reaction cannot proceed at all (**Fig. 3c**
192 **and d**). The introduction of CCl_4 as an electron scavenger almost terminates the H_2 production, and
193 moreover, the generation of EG or GLD is decelerated considerably once adding triethanolamine
194 (TEOA) as a hole scavenger, indicating the joint participation of photogenerated electrons and holes in
195 the evolution of H_2 and EG/GLD. In addition, comparative reaction with EG employed as the reactant
196 was performed to investigate the possible consecutive oxidation of EG. Notably, no product is
197 detected over both Ni_1-CdS/SiO$_2$ and Ni_n-CdS/SiO$_2$ during the experimental process, which suggests
198 that EG can exist stably and GLD is not originated from the overoxidation of EG. Furthermore, the
199 time-dependent product distributions for the dehydrocoupling of methanol illustrate that the
200 production of EG over Ni_1-CdS/SiO$_2$ increases as the reaction time extends (**Fig. 3e**). An induction
201 period is clearly observed, since stabilizing both the adsorption-desorption equilibrium of reactants
202 (i.e., methanol molecules) on the catalyst surface and the accumulation of initial reaction
203 intermediates demands a short duration. Meanwhile, the yields of GLD and HCHO exhibit an upward
204 trend, albeit with extremely low values during the reaction process. In contrast, although HCHO also
205 maintains a relatively low output over Ni_n-CdS/SiO$_2$, its generation presents a trend of first increasing
206 and then decreasing with the reaction proceeding (**Fig. 3f**), which indicates that in this catalytic system,
207 HCHO is not a by-product but an intermediate for the production of target product GLD.

208 To gain further insights, in-situ electron paramagnetic resonance (EPR) spectroscopic studies were
209 adopted to monitor the radical intermediates involved in the dehydrocoupling of methanol using 5,5-
210 dimethyl-1-pyrroline *N*-oxide (DMPO) as a spin-trapping reagent (**Fig. 3g**). Under light irradiation, the
211 generated •CH$_2$OH radical is trapped by DMPO, as manifested by the characteristic peaks belonging to
212 the DMPO-CH$_2$OH adduct[1]. Upon Ni decoration, an obvious increase in the evolution rate of •CH$_2$OH
213 radical is observed over Ni_1-CdS/SiO$_2$ and Ni_n-CdS/SiO$_2$, indicating that Ni species significantly
214 promotes the cleavage of α-C−H bond in methanol. It is noted that the methoxyl (CH$_3$O•) radical,
215 commonly generated in the conversion of methanol[1,17], is absent in the EPR spectra, which is maybe
216 due to the small amount of CH$_3$O• radical generated in this catalytic system as well as its short-lived
217 nature[1]. In addition, through the in-situ capture of •CH$_2$OH radical by 1,1-diphenylethylene (DPE)[18],
218 the product of 3,3-diphenylpropan-1-ol (DPE-CH$_2$OH) is obtained over Ni_1-CdS/SiO$_2$, with a selectivity
219 of 95% according to the gas chromatography results (**Fig. 3h**, **Supplementary Fig. 21** and **22**). Another
220 trace product of 3-methoxy-3,3-diphenylpropan-1-ol (CH$_3$O-DPE-CH$_2$OH) is attributed to the addition

5

221 of methoxy radical (CH$_3$O•) to DPE-CH$_2$OH. These findings illustrate that the preferential cleavage of α-
222 C−H bond to generate •CH$_2$OH radical in methanol than the O−H bond occurs readily on Ni$_1$-CdS/SiO$_2$,
223 thereby generating EG via •CH$_2$OH radical coupling[1,18]. By contrast, for the case over Ni$_n$-CdS/SiO$_2$,
224 capturing radicals by DPE affords the products of DPE-CH$_2$OH and CH$_3$O-DPE-CH$_2$OH with selectivities
225 of 79% and 21%, respectively—corresponding to the radical selectivities of 83% for •CH$_2$OH radical and
226 17% for CH$_3$O• radical, indicating that the cleavage of both α-C−H and O−H bond in methanol occurs
227 concurrently on Ni$_n$-CdS/SiO$_2$. This distinctly enhanced generation of CH$_3$O• radical originating from
228 O−H cleavage of methanol is answerable for the formation of HCHO intermediate[42]. As corroborated
229 by the dynamic trend of HCHO yield (first increasing and then decreasing) observed in **Fig. 3f**, the as-
230 generated HCHO intermediate subsequently reacts with the •CH$_2$OH radical to afford GLD via the Ni
231 clusters-assisted addition-elimination mechanism, as further confirmed by our theoretical calculations
232 below.

233 Upon gathering the above results, DFT calculations were further carried out to shed light on the
234 selectivity regulation between EG and GLD synthesis and the overall reaction pathways for the
235 dehydrocoupling of methanol over Ni$_1$-CdS/SiO$_2$ and Ni$_n$-CdS/SiO$_2$. Based on the EXAFS analysis, single
236 Ni atoms and Ni clusters coordinated with the capping molecule of MPA on the surface of CdS QDs are
237 selected to represent the catalytic sites on Ni$_1$-CdS/SiO$_2$ and Ni$_n$-CdS/SiO$_2$, respectively
238 (**Supplementary Fig. 23-26**). As sketched in **Fig. 4a**, both methanol adsorption steps over Ni$_1$-CdS/SiO$_2$
239 and Ni$_n$-CdS/SiO$_2$ composite are thermodynamically downhill with the values of −0.056 and −0.453 eV,
240 respectively. For the Ni single atom-assisted catalytic mechanism, the first deprotonation step of
241 methanol over Ni$_1$-CdS/SiO$_2$ is endergonic to afford •CH$_2$OH radical via overcoming the relative energy
242 of 0.494 eV. Subsequently, a homo-coupling pathway for EG production is thermodynamically
243 favorable (0.015 eV) compared with the addition-elimination mechanism for GLD production (0.702 eV)
244 or the second deprotonation route for HCHO production (1.135 eV). Under the catalytic mechanism
245 supported by the Ni cluster, the homo-coupling of •CH$_2$OH radical is exothermic with the values of
246 −0.368 eV; nevertheless, the desorption step of EG is considerably more difficult owing to the high
247 relative energy of 1.095 eV. On the contrary, a thermodynamically more feasible reaction pathway is
248 that, the •CH$_2$OH radical undergoes an addition-elimination pathway with a negligible condensation
249 energy of 0.090 eV, followed by an exergonic deprotonation to produce GLD (−0.539 eV). The
250 desorption process of GLD is regarded as the rate-limiting step by overcoming a moderate relative
251 energy of 0.633 eV. Taking the above theoretical and experimental results into account together, the
252 overall catalytic reaction mechanism for highly selective and divergent synthesis of EG and GLD over
253 Ni$_1$-CdS/SiO$_2$ with single Ni atoms and Ni$_n$-CdS/SiO$_2$ with Ni clusters is put forward correspondingly, as
254 displayed in **Fig. 4b**.

255 **Discussion**

256 In summary, we report the efficient photoredox-catalyzed dehydrocoupling of methanol into tunable
257 EG by a radical homo-coupling pathway and GLD by a radical addition-elimination pathway over the
258 different atomically dispersed Ni-decorated CdS/SiO$_2$ composite under ambient conditions. EG (90%
259 selectivity) and GLD (96% selectivity) are preferentially generated over Ni$_1$-CdS/SiO$_2$ with single Ni
260 atoms and Ni$_n$-CdS/SiO$_2$ with Ni clusters, respectively, along with excellent reactivity compared with
261 other catalytic systems. Mechanistic insights into the divergent synthesis of EG and GLD are proposed
262 based on joint experimental results and DFT calculations. The structure-performance relationship
263 established over atomically dispersed Ni cocatalysts advances our understanding of catalyst design for
264 methanol conversion, paving the way for future progress in devising catalysts for efficient and divergent

265 synthesis of sustainable chemicals.

266 **Methods**

267 **Catalyst preparation.** Synthesis of Ni-CdS/SiO$_2$ composite: Ni-CdS/SiO$_2$ was prepared based on a facile
268 photodeposition strategy. Typically, 50 mg of CdS/SiO$_2$ was dissolved in a 50 mL of mixed solution of
269 deionized (DI) water (40 mL) and ethanol (10 mL) that contained a certain amount of NiCl$_2$·6H$_2$O (17.04
270 μmol/mL (that is 1 mg$_{Ni}$/mL), 50 μL, 100 μL, 250 μL and 500 μL). Subsequently, the suspension was
271 irradiated with a 300 W xenon lamp (PLS-SXE 300D, Beijing Perfectlight Co., Ltd.) under nitrogen (N$_2$)
272 atmosphere for 0.5 h. The obtained products were collected via centrifugation and washed by DI water.
273 Followed by blow-drying with N$_2$, the Ni-CdS/SiO$_2$ composites with different Ni weight loading (0.1%,
274 0.2%, 0.5% and 1.0%) were obtained.

275 **Photoactivity testing.** Selective dehydrocoupling of methanol to EG or GLD integrated with H$_2$
276 generation was carried out in a double-walled quartz reactor, which was maintained at 25 °C by a flow
277 of circulating water. Typically, 20 mg of sample was added into 10 mL methanol. The reaction solution
278 was purged with Ar gas for 15 min. Then, a 300 W xenon lamp (PLS-SXE 300D, Beijing Perfectlight Co.,
279 Ltd.) was used as light source, and the light power density is measured to be approximately 0.18 W
280 cm^{-2}. The generated H$_2$ was quantified by a gas chromatography (Shimadzu GC-8A 2014C), and EG or
281 GLD was analyzed by the gas chromatography-mass spectrometry. In addition, the by-product of HCHO
282 was quantified by the acetylacetone colorimetric determination method, which can be found in
283 Supporting Information.

284 **Computational details.** The present first principle DFT calculations were performed by Vienna Ab initio
285 Simulation Package (VASP) with the projector augmented wave (PAW) method[43]. The exchange-
286 functional was treated using the generalized gradient approximation (GGA) of Perdew-Burke-Emzerhof
287 (PBE) functional[44]. The Spin-polarizations were carried out for all calculations. The energy cutoff for the
288 plane wave basis expansion was set to 450 eV and the force on each atom less than 0.05 eV/Å was set
289 for convergence criterion of geometry relaxation. The Brillouin zones (BZ) were sampled by using the
290 surfaces structures of 2 × 2 × 1 Monkhorst-Pack K point. The self-consistent calculations apply a
291 convergence energy threshold of 10^{-5} eV. The DFT-D3 method was employed to consider the van der
292 Waals interaction. A 15 Å vacuum was added along the z direction in order to avoid the interaction
293 between periodic structures. In addition, the lattice parameters of the two models are consistent, with
294 a = b = 16.803 Å, c = 33.182 Å, α = β = 90°, and γ = 120°. Structural relaxation calculations were
295 performed for all structures, and the convergence criteria for energy and force mentioned earlier were
296 satisfied. During the optimization process, the bottom two atomic layers were fixed to simulate the
297 properties of the bulk phase, while all remaining atoms were allowed to relax freely. The free energies
298 of the reaction steps were calculated by the equation:

299 $$\Delta G = \Delta E_{DFT} + \Delta E_{ZPE} - T\Delta S$$

300 where ΔE_{DFT} is the DFT electronic energy difference of each step, ΔE_{ZPE} and ΔS are the correction of
301 zero-point energy and the variation of entropy, respectively, which are obtained by vibration analysis,
302 T is the temperature (T = 300 K). The details of Zero-Point Energy (ZPE) correction and entropy values
303 are supplemented in **Supplementary Table 8**.

304 **Data availability**

305 The data that support the findings of this study are available from the corresponding author upon
306 request.

307 **Acknowledgements**

Competing interests

The authors declare no competing financial interests.

References

1. Xie, S. *et al.* Visible light-driven C-H activation and C-C coupling of methanol into ethylene glycol. *Nat. Commun.* **9**, 1181 (2018).

2. Jiao, J. *et al.* Sun-simulated-driven production of high-purity methanol from carbon dioxide. *Nat. Commun.* **16**, 857 (2025).

3. Yang, H. *et al.* Potential-driven structural distortion in cobalt phthalocyanine for electrocatalytic CO_2/CO reduction towards methanol. *Nat. Commun.* **15**, 7703 (2024).

4. Moran, J., Preetz, A., Mesch, R. A. & Krische, M. J. Iridium-catalysed direct C-C coupling of methanol and allenes. *Nat. Chem.* **3**, 287-290 (2011).

5. Graciani, J. *et al.* Highly active copper-ceria and copper-ceria-titania catalysts for methanol synthesis from CO_2. *Science* **345**, 546-550 (2014).

6. Dummer, N. F. *et al.* Methane Oxidation to Methanol. *Chem. Rev.* **123**, 6359-6411 (2023).

7. Olsbye, U. *et al.* Conversion of Methanol to Hydrocarbons: How Zeolite Cavity and Pore Size Controls Product Selectivity. *Angew. Chem. Int. Ed.* **51**, 5810-5831 (2012).

8. Olah, G. A. Towards Oil Independence Through Renewable Methanol Chemistry. *Angew. Chem. Int. Ed.* **52**, 104-107 (2013).

9. Lu, K. *et al.* High Ethylene Selectivity in Methanol-to-Olefin (MTO) Reaction over MOR-Zeolite Nanosheets. *Angew. Chem. Int. Ed.* **59**, 6258-6262 (2020).

10. Kamat, P. V. & Jin, S. Semiconductor Photocatalysis: "Tell Us the Complete Story!". *ACS Energy Lett.* **3**, 622-623 (2018).

11. Qi, M.-Y., Conte, M., Anpo, M., Tang, Z.-R. & Xu, Y.-J. Cooperative coupling of oxidative organic synthesis and hydrogen production over semiconductor-based photocatalysts. *Chem. Rev.* **121**, 13051-13085 (2021).

12. Chen, X., Shen, S., Guo, L. & Mao, S. S. Semiconductor-based Photocatalytic Hydrogen Generation. *Chem. Rev.* **110**, 6503-6570 (2010).

13. Cheng, J.-K. & Loh, T.-P. Copper- and Cobalt-Catalyzed Direct Coupling of sp^3 α-Carbon of Alcohols with Alkenes and Hydroperoxides. *J. Am. Chem. Soc.* **137**, 42-45 (2015).

14. Zhang, S.-Y., Zhang, F.-M. & Tu, Y.-Q. Direct Sp^3 α-C–H activation and functionalization of alcohol and ether. *Chem. Soc. Rev.* **40**, 1937-1949 (2011).

15. Qi, M.-Y., Li, Y.-H., Anpo, M., Tang, Z.-R. & Xu, Y.-J. Efficient Photoredox-Mediated C-C Coupling Organic Synthesis and Hydrogen Production over Engineered Semiconductor Quantum Dots. *ACS Catal.* **10**, 14327-14335 (2020).

16. Peng, Y. *et al.* Photocatalytic synthesis of ethylene glycol and hydrogen from methyl tert-butyl ether. *Nat. Commun.* **16**, 3959 (2025).

350 17 Wang, L. *et al.* Precisely Constructed Metal Sulfides with Localized Single-Atom Rhodium for
351 Photocatalytic C–H Activation and Direct Methanol Coupling to Ethylene Glycol. *Adv. Mater.* **35**,
352 2205782 (2023).

353 18 Luo, N. *et al.* Low-Work Function Metals Boost Selective and Fast Scission of Methanol C–H
354 Bonds. *ACS Catal.* **12**, 6375-6384 (2022).

355 19 Zhang, H. *et al.* C-H activations of methanol and ethanol and C-C couplings into diols by zinc-
356 indium-sulfide under visible light. *Chem. Commun.* **56**, 1776-1779 (2020).

357 20 Wang, L. *et al.* Solar energy-driven C–H activation of methanol for direct C–C coupling to
358 ethylene glycol with high stability by nitrogen doped tantalum oxide. *Chin. J. Catal.* **42**, 1459-
359 1467 (2021).

360 21 Liang, J. *et al.* Oxygen-Activated Boron Nitride for Selective Photocatalytic Coupling of
361 Methanol to Ethylene Glycol. *Angew. Chem. Int. Ed.* **63**, e202318236 (2024).

362 22 Luo, J. *et al.* Photocatalytic Methanol Dehydrogenation with Switchable Selectivity. *J. Am.*
363 *Chem. Soc.* **147**, 3428-3437 (2025).

364 23 Faveere, W. H. *et al.* Toward Replacing Ethylene Oxide in a Sustainable World: Glycolaldehyde
365 as a Bio-Based C_2 Platform Molecule. *Angew. Chem. Int. Ed.* **60**, 12204-12223 (2021).

366 24 Garrabou, X. *et al.* Asymmetric Self- and Cross-Aldol Reactions of Glycolaldehyde Catalyzed by
367 D-Fructose-6-phosphate Aldolase. *Angew. Chem. Int. Ed.* **48**, 5521-5525 (2009).

368 25 Powner, M. W., Zheng, S.-L. & Szostak, J. W. Multicomponent Assembly of Proposed DNA
369 Precursors in Water. *J. Am. Chem. Soc.* **134**, 13889-13895 (2012).

370 26 Faveere, W. *et al.* Glycolaldehyde as a Bio-Based C_2 Platform Chemical: Catalytic Reductive
371 Amination of Vicinal Hydroxyl Aldehydes. *ACS Catal.* **10**, 391-404 (2020).

372 27 Zhang, N. *et al.* Near-field dielectric scattering promotes optical absorption by platinum
373 nanoparticles. *Nat. Photonics* **10**, 473-482 (2016).

374 28 Qi, M.-Y. & Xu, Y.-J. Efficient and Direct Functionalization of Allylic sp^3 C–H Bonds with
375 Concomitant CO_2 Reduction. *Angew. Chem. Int. Ed.* **62**, e202311731 (2023).

376 29 Qi, M.-Y., Conte, M., Tang, Z.-R. & Xu, Y.-J. Engineering semiconductor quantum dots for
377 selectivity switch on high-performance heterogeneous coupling photosynthesis. *ACS Nano* **16**,
378 17444-17453 (2022).

379 30 Zang, W. *et al.* Efficient hydrogen evolution of oxidized $Ni-N_3$ defective sites for alkaline
380 freshwater and seawater electrolysis. *Adv. Mater.* **33**, 2003846 (2021).

381 31 Lin, L. *et al.* Atomically dispersed Ni/alpha-MoC catalyst for hydrogen production from
382 methanol/water. *J. Am. Chem. Soc.* **143**, 309-317 (2021).

383 32 Xia, C. *et al.* General synthesis of single-atom catalysts with high metal loading using graphene
384 quantum dots. *Nat. Chem.* **13**, 887-894 (2021).

385 33 Qian, G. *et al.* Efficient photoreduction of diluted CO_2 to tunable syngas by Ni-Co dual sites
386 through d-band center manipulation. *Angew. Chem. Int. Ed.* **61**, e202210576 (2022).

387 34 Denisov, N. *et al.* Light-Induced Agglomeration of Single-Atom Platinum in Photocatalysis. *Adv.*
388 *Mater.* **35**, 2206569 (2023).

389 35 Sarma, B. B., Maurer, F., Doronkin, D. E. & Grunwaldt, J.-D. Design of Single-Atom Catalysts and
390 Tracking Their Fate Using Operando and Advanced X-ray Spectroscopic Tools. *Chem. Rev.* **123**,
391 379-444 (2023).

392 36 Yang, J., Wang, D., Han, H. & Li, C. Roles of Cocatalysts in Photocatalysis and
393 Photoelectrocatalysis. *Acc. Chem. Res.* **46**, 1900-1909 (2013).

394 37 Li, X., Yu, J., Jaroniec, M. & Chen, X. Cocatalysts for selective photoreduction of CO_2 into solar
395 fuels. *Chem. Rev.* **119**, 3962-4179 (2019).
396 38 Yan, X. *et al.* An electron-hole rich dual-site nickel catalyst for efficient photocatalytic overall
397 water splitting. *Nat. Commun.* **14**, 1741 (2023).
398 39 Lu, Q. *et al.* One-pot synthesis of interconnected $Pt_{95}Co_5$ nanowires with enhanced
399 electrocatalytic performance for methanol oxidation reaction. *Nano Res.* **11**, 2562-2572 (2018).
400 40 Kakati, N. *et al.* Anode Catalysts for Direct Methanol Fuel Cells in Acidic Media: Do We Have
401 Any Alternative for Pt or Pt–Ru? *Chem. Rev.* **114**, 12397-12429 (2014).
402 41 Liu, J. *et al.* Designing Nanoporous Coral-Like Pt Nanowires Architecture for Methanol and
403 Ammonia Oxidation Reactions. *Adv. Funct. Mater.* **32**, 2110702 (2022).
404 42 Fan, Y. *et al.* Photocatalytic Coupling of Methanol and Formaldehyde into Ethylene Glycol with
405 High Atomic Efficiency. *Catal. Lett.* **148**, 2274-2282 (2018).
406 43 Blöchl, P. E. Projector augmented-wave method. *Phys. Rev. B* **50**, 17953-17979 (1994).
407 44 Perdew, J. P. *et al.* Atoms, molecules, solids, and surfaces: Applications of the generalized
408 gradient approximation for exchange and correlation. *Phys. Rev. B* **46**, 6671-6687 (1992).

409
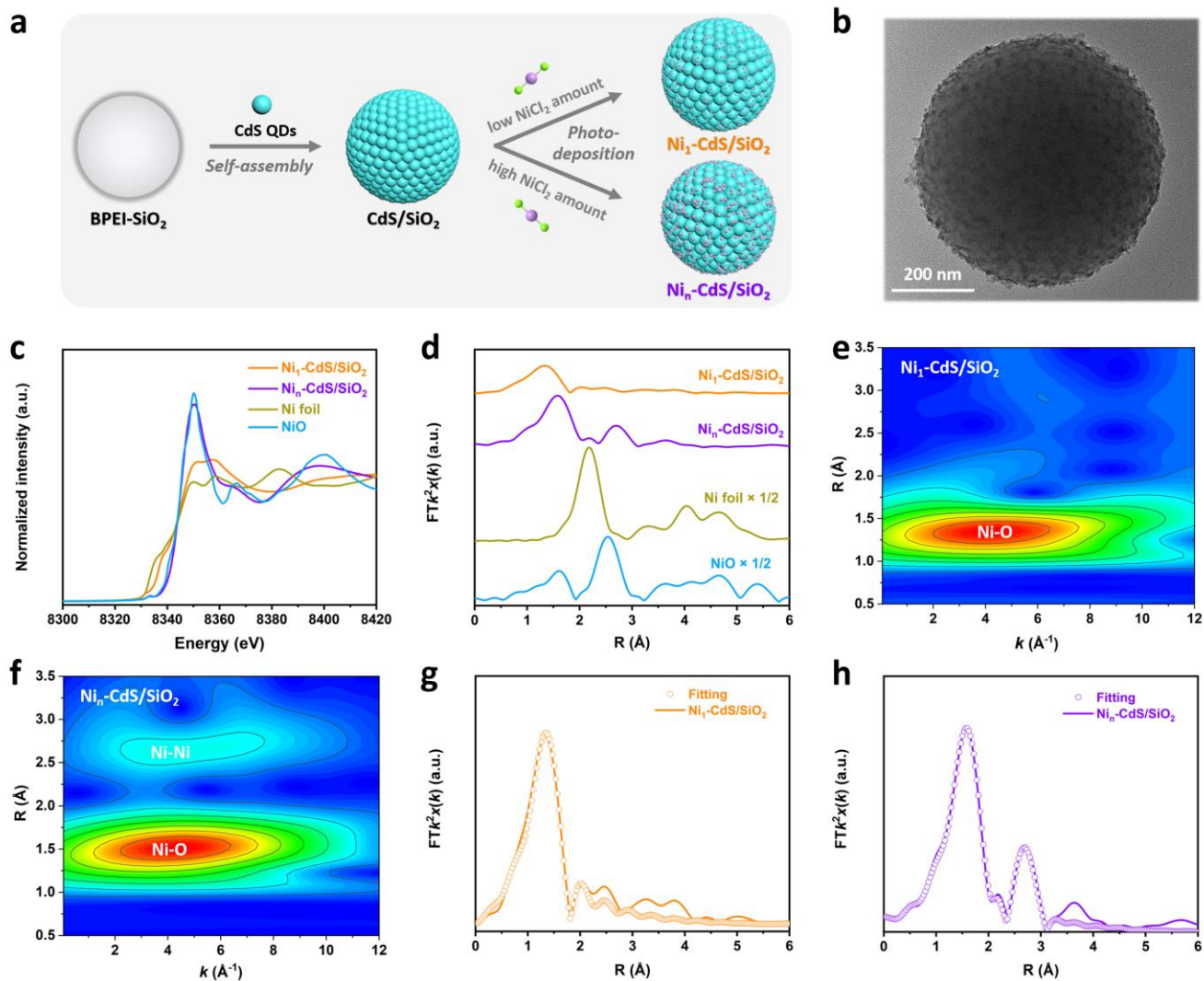
Fig. 1 | Preparation and characterization of Ni-CdS/SiO₂ with atomically dispersed Ni species. a, Synthesis procedure for the Ni-CdS/SiO₂ composite. **b**, TEM image of CdS/SiO₂ composite, **c,d** Normalized Ni K-edge XANES spectra (**c**) and FT-EXAFS spectra (**d**) of Ni-CdS/SiO₂ along with Ni foil and NiO as references. Wavelet transform for Ni K-edge EXAFS spectra of (**e**) Ni₁-CdS/SiO₂ and (**f**) Niₙ-CdS/SiO₂. **g,h**, EXAFS fitting curves for (**g**) Ni₁-CdS/SiO₂ with single Ni atoms and (**h**) Niₙ-CdS/SiO₂ with Ni clusters.
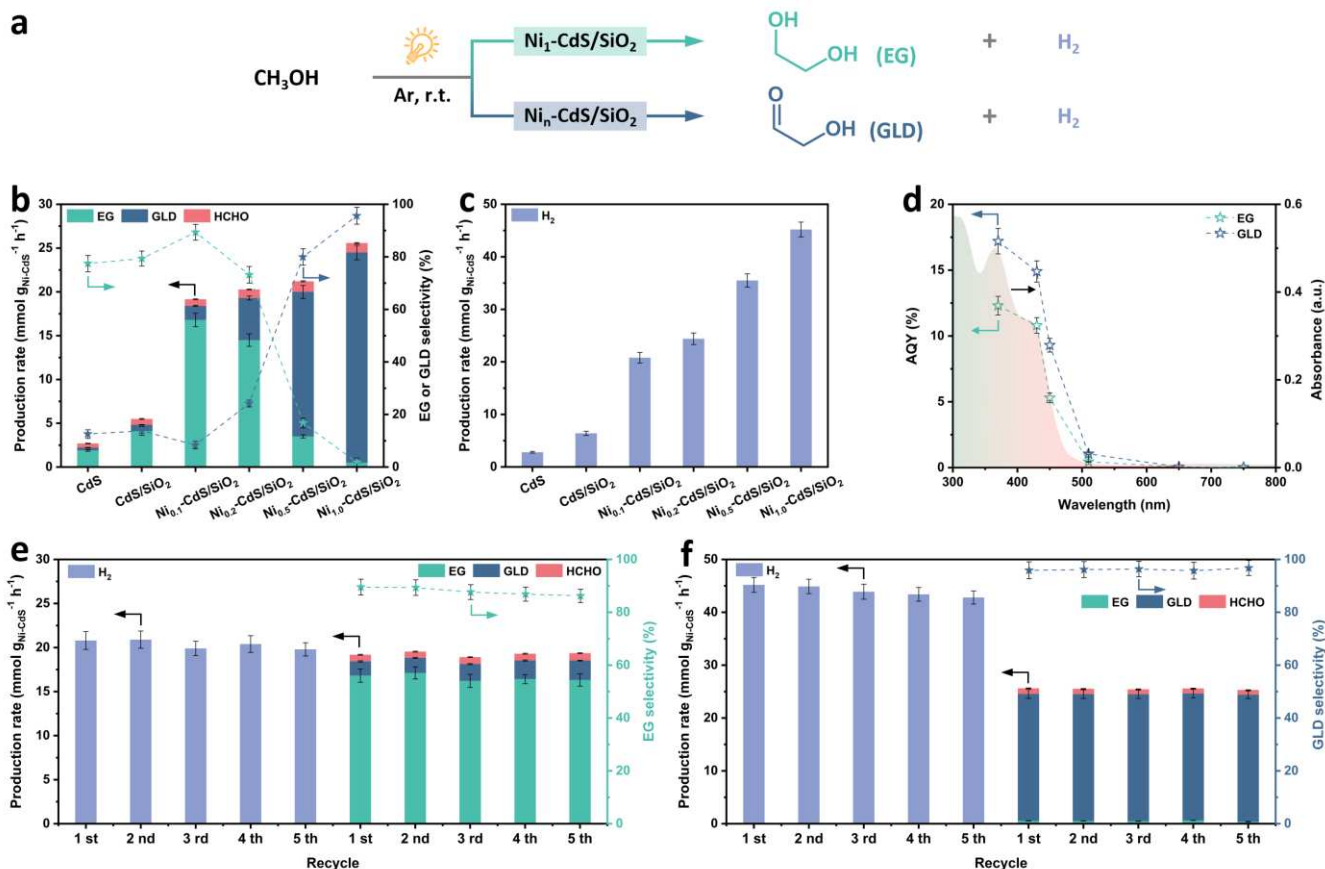
**Fig. 2 | Selective switchable dehydrocoupling of methanol to produce EG or GLD. a**, Schematic representation of the chemical reactions for conversion of methanol into EG or GLD as well as H_2. **b**, Production rate of various products and EG or GLD selectivity over CdS, CdS/SiO_2 and $Ni-CdS/SiO_2$ composites with different Ni loading amounts. **c**, H_2 production rate over CdS, CdS/SiO_2 and $Ni-CdS/SiO_2$ composites with different Ni loading amounts. Standard conditions: 20 mg catalyst in 10 mL of methanol solution, Ar atmosphere, 300 W xenon lamp, 10 h, room temperature. **d**, Diffuse reflectance spectroscopy (DRS) spectrum of CdS/SiO_2 composite and AQYs for EG or GLD production over $Ni-CdS/SiO_2$ composite under different monochromatic lights. **e,f**, Recycling performance of (**e**) Ni_1-CdS/SiO_2 composite with single Ni atoms and (**f**) Ni_n-CdS/SiO_2 composite with Ni clusters.

12
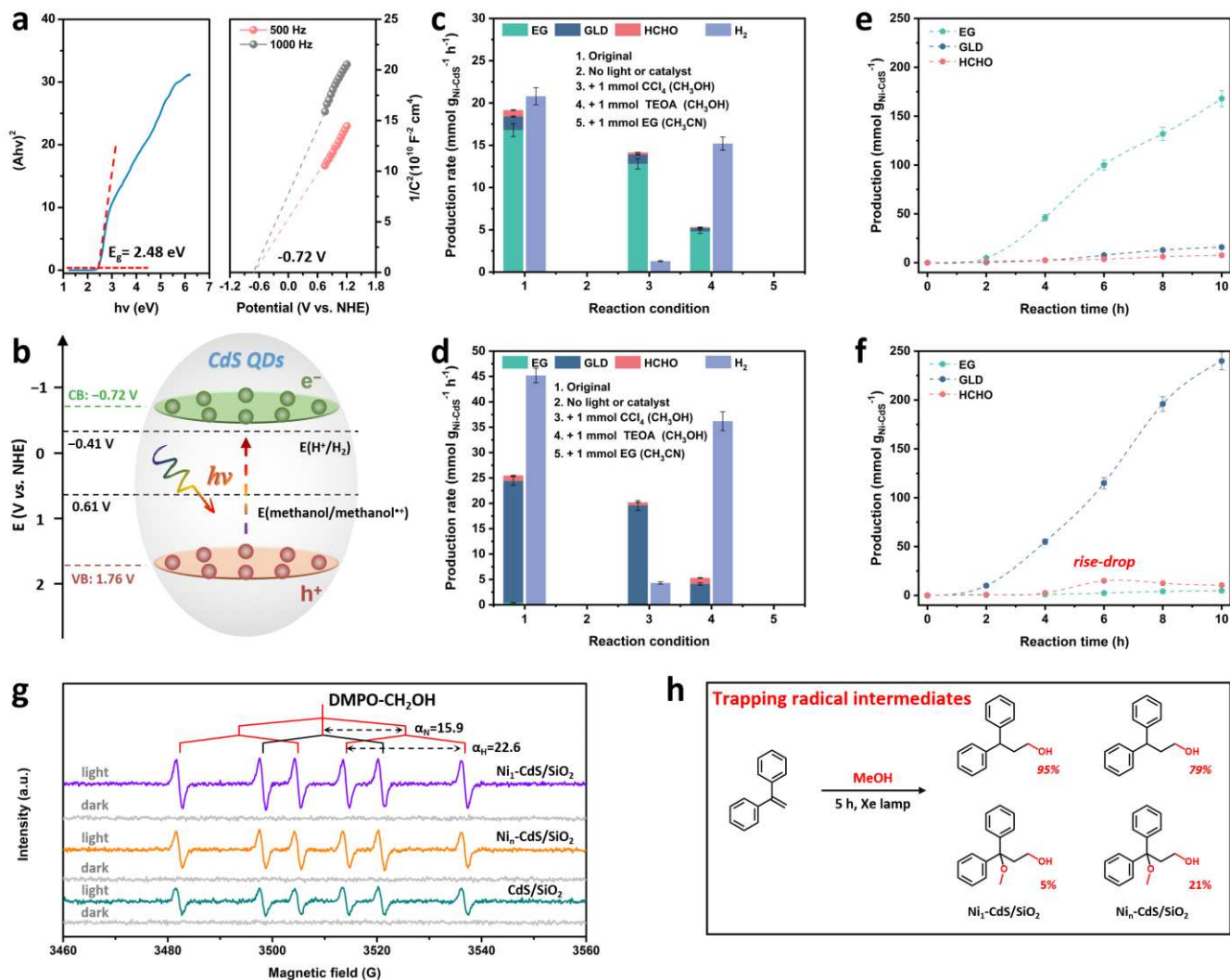
427
428 **Fig. 3 | Mechanism insight for dehydrocoupling of methanol. a**, Tauc plot (left) and Mott-Schottky
429 plots (right) for CdS QDs. **b**, Redox potentials of methanol oxidation and H_2 evolution against the VB
430 and CB edges of CdS QDs. **c,d**, Control experiments with different additives catalyzed by (**c**) Ni_1-
431 CdS/SiO_2 and (**d**) Ni_n-CdS/SiO_2 composite. Standard conditions: 20 mg catalyst in 10 mL of CH_3OH
432 (entries 1-4) or CH_3CN solution (entry 5), Ar atmosphere, 300 W xenon lamp, 10 h, room temperature.
433 **e,f**, Time profiles of products evolution over (**e**) Ni_1-CdS/SiO_2 and (**f**) Ni_n-CdS/SiO_2 composite. **g**, In-situ
434 EPR spectra of CdS/SiO_2, Ni_1-CdS/SiO_2 and Ni_n-CdS/SiO_2 composite in Ar saturated methanol solution in
435 the presence of DMPO. **h**, Capturing radical intermediates by DPE in dehydrocoupling of methanol.
436 Standard conditions: 20 mg catalyst in 10 mL of CH_3OH solution with 1 mmol of 1,1-diphenylethylene,
437 Ar atmosphere, 300 W xenon lamp, 5 h, room temperature.
438

13

439
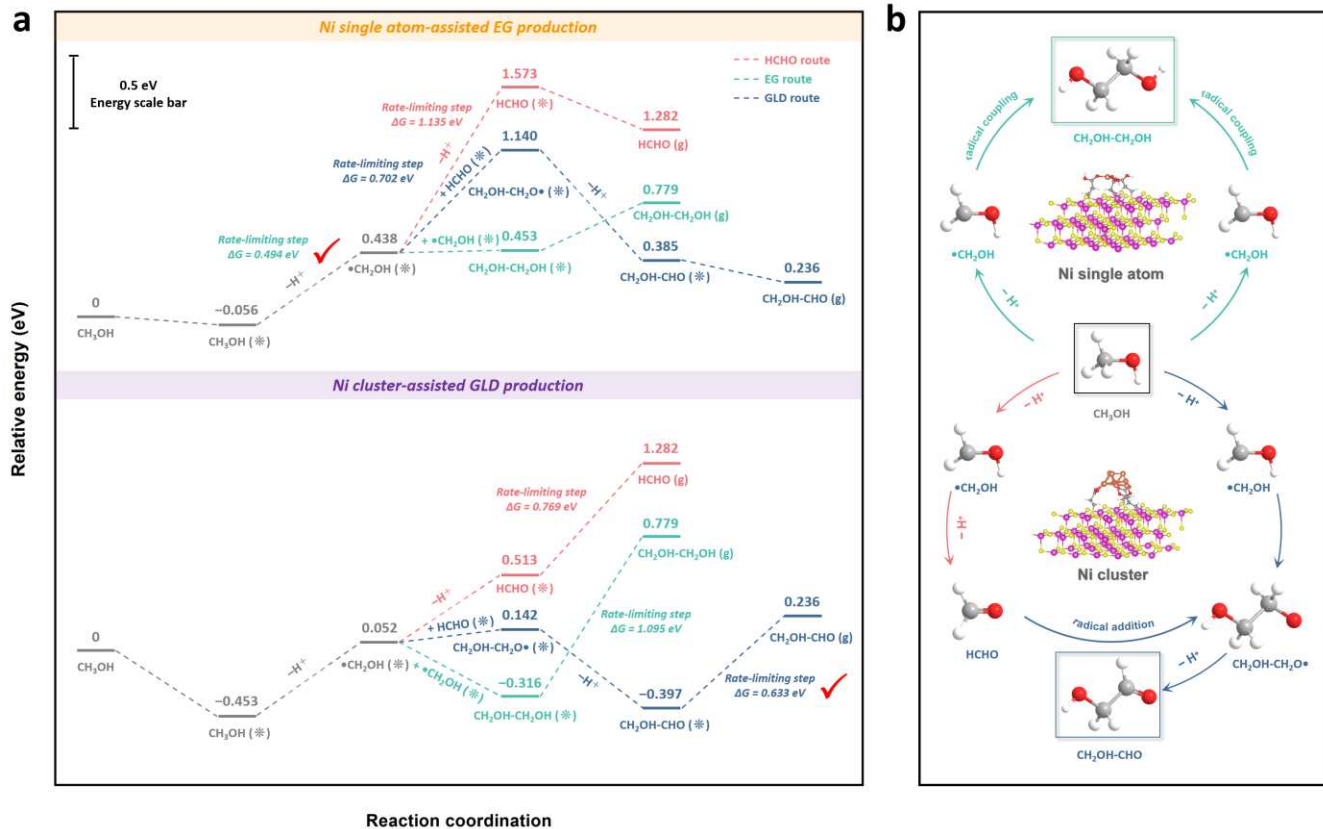
Fig. 4 | DFT calculations and proposed mechanism. a, Calculated potential energy diagrams for dehydrocoupling of methanol catalyzed by Ni_1-CdS/SiO$_2$ with Ni single atoms and Ni_n-CdS/SiO$_2$ with Ni clusters, respectively. **b**, Proposed mechanism for switchable methanol C−C coupling to EG or GLD.

14